Assessment of the structural representativeness of sample data sets for the mechanical characterization of deep formations.

GEOPHYSICS, VOL. 80, NO. 5 (SEPTEMBER-OCTOBER 2015); P. D441–D457, 22 FIGS., 4 TABLES.
10.1190/GEO2014-0351.1

Assessment of the structural representativeness of sample data sets for the mechanical characterization of deep formations

Guido Musso[1], Renato Maria Cosentini[1], Sebastiano Foti[1], Cesare Comina[2], and Gaia Capasso[3]

ABSTRACT

Accurate characterization of the mechanical behavior of geomaterials at depth is a fundamental need for geologic and engineering purposes. Laboratory tests on samples from well cores provide the material characterization in terms of mechanical response and other relevant properties. Representativeness of a sample data set with respect to the in situ conditions at depth is a key issue, which needs to be addressed to extrapolate the laboratory response to the whole rock mass. We have developed a procedure aimed at quantitatively evaluating the representativeness of laboratory samples. The methodology is based on joint processing of laboratory ultrasonic tests and wellbore sonic logs. A structural index is used to quantify the difference between the average structure of the laboratory sample and the structure of the formation at the wellbore scale. This index could be used to identify different causes of discrepancies between the behavior of the cored samples and the behavior of the rock formation as documented by well logs. Then, it could also be used to integrate laboratory data for the construction of a reliable geomechanical model with reference to the real in situ state. The methodology was applied to three different experimental data sets, showing the effectiveness of the method.

INTRODUCTION

Mechanical characterization of rock formations at great depth is a key factor for geomechanical aspects of energy production, such as the exploitation of gas and oil reservoirs, of geothermal energy, and to geoenvironmental issues, e.g., CO_2 sequestration. For instance, in oil-related applications, a reliable identification of rock behavior is crucial for reservoir-scale modeling (evaluation of subsidence and of cap-rock integrity), well-scale modeling (open-hole stability and cased-hole integrity analyses), and intermediate scale modeling (stimulation/injection operations and hydraulic fracturing campaigns).

State-of-the-art computational tools and advanced constitutive laws allow 3D simulations of these complex hydromechanical problems. Accuracy of predictions is governed by a reliable characterization of the in situ state and of the mechanical response of the geomaterial in the stress-strain range involved.

Laboratory tests can provide an accurate characterization of the mechanical behavior of rock samples because they are performed under well-controlled conditions (stress state, stress path, pore-fluid pressure, temperature, and chemistry). Nevertheless, a comprehensive geomechanical characterization cannot rely only on laboratory tests: rock samples are usually limited in number, and their mechanical response may be not representative of in situ behavior.

Limited representativeness depends on the scale of investigation and on differences between the structure of the samples and the structure of the rock formation (e.g., Fjær et al., 2008). On one hand, the spacing of fractures and joints in the formation, having significant impact on engineering work, can exceed the size of the samples (megastructural effects). On the other hand, the original rock fabric can be altered by coring and subsequent sample preparation, especially for unconsolidated and weakly cemented sediments (microstructural effects), as extensively documented in the literature (e.g., Holt et al., 2000; Fjær et al., 2008; Alvarado et al., 2012). Holt et al. (2000) reproduce damage due to coring with laboratory experiments. Artificial weakly cemented sandstones consolidated at high stress levels ("virgin" state) were first exposed to sudden stress release (coring) and then reloaded to evaluate changes induced on the mechanical and dynamic parameters of the rock. This simulated coring significantly reduced the uniaxial compressive strength and the oedometer modulus. Elastic-wave

Manuscript received by the Editor 31 July 2014; revised manuscript received 1 April 2015; published online 16 July 2015.
[1]Politecnico di Torino, Dipartimento di Ingegneria Strutturale Edile e Geotecnica, Torino, Italy. E-mail: guido.musso@polito.it; renato.cosentini@polito.it; sebastiano.foti@polito.it.
[2]Università degli Studi di Torino, Dipartimento di Scienze della Terra, Torino, Italy. E-mail: cesare.comina@unito.it.
[3]Eni E&P, TEOF, S. Donato Milanese, Italy. E-mail: gaia.capasso@eni.com.

velocities measured under loaded conditions in the cored samples were also smaller than those measured in virgin samples, although the difference between the velocities obtained for the two reference states decreased with the stress increase. Other researchers (e.g., Martin and Stimpson, 1994; Eberhardt et al., 1999) have obtained similar results.

In situ measurements can provide information on the rock properties when they are not affected by coring effects. Sonic logs have the advantage of providing continuous measurements of the velocity of elastic waves along the formation. Moreover, given the distance between the sensors used to measure elastic velocities (from tens of centimeters to meters), the recordings also take into account the presence of fractures or joints. A drawback of sonic logs is that they investigate a narrow strain range because only very small strains are induced by wave propagation, whereas the mechanical response can depend heavily on strain magnitude. Thus, although a complete mechanical characterization remains based on laboratory tests, information from sonic logs can help to evaluate whether samples selected for laboratory tests are representative of the original rock formation and also to extend the characterization to depths at which no samples are taken. A link between sonic logs and mechanical laboratory tests is then needed to extend the response given by the sonic log to the strain range investigated by the laboratory tests, with the aim of obtaining a reliable and complete geomechanical characterization. However, the integration of laboratory and well measurements is not straightforward because the effect of varying state parameters (stress, porosity, saturation, and structure) and of frequency-dependent dispersion are to be considered.

A quantitative evaluation of the representativeness of laboratory sample data sets can be based on joint processing of laboratory ultrasonic velocity tests and wellbore sonic logs. Joint processing also allows the mechanical behavior defined with laboratory investigation to be extrapolated for building a geomechanical model appropriate for the scale and the stress state concerned. After a detailed description of the procedure proposed, the application to three experimental data sets is reported.

EVALUATION OF SAMPLE REPRESENTATIVENESS

The proposed methodology is based on joint processing of laboratory ultrasonic tests and wellbore sonic logs. In particular, the stress dependence of elastic-wave velocities is determined at the laboratory scale, extrapolated to the log scale, and finally compared with available sonic logs. The methodology can be based either on P- or on S-wave velocities. Although this study focuses on isotropic cases, its extension to anisotropic media is relatively straightforward when wave velocities obtained along different directions of propagation are available to estimate anisotropy effects.

Data processing is described in the following paragraphs.

Dependence of elastic-wave velocities on stress state and structure

The dependence of elastic-wave velocities on the effective stress (i.e., the difference between the confining stress and the pore pressure) is well established in the rock-physics literature. The velocity-effective stress relationship is nonlinear with a steeper increase in velocity with effective stress at low confinements and a smoother increase at higher confinements. This dependence can be explained considering closure of ubiquitous mechanical microdefects (Brich, 1960, 1961; Walsh, 1965a, 1965b), or otherwise, for granular materials, in terms of increase of the contact area between grains (e.g., Mindlin, 1949).

Several equations, mostly empirical, have been proposed to describe stress dependence of the compressional (P) and shear (S) wave velocities (e.g., Zimmerman et al., 1986; Eberhart-Phillips et al., 1989; Freund, 1992; Wang et al., 2005). These relationships provide a good approximation of the observed velocity variations with effective stress, although mostly relying only on phenomenological parameters.

One of the simplest physically based models is the Hertz-Mindlin one (e.g., Mavko et al., 2009). This model is based on the theoretical behavior of spherical particles, but experimental evidences suggest that Hertz-Mindlin-like expressions can correctly quantify the stress sensitivity of wave velocities in rocks (Cha et al., 2009; Rasolofosaon and Zinszner, 2012). According to the Hertz-Mindlin model, the stress dependence of elastic-wave velocity V_i is described by a power law:

$$V_i = \alpha_i \left(\frac{p'}{p'_0} \right)^{\beta_i}, \tag{1}$$

where i denotes the type of wave considered (P or S), p' is the isotropic effective stress, p'_0 is the reference isotropic effective stress (throughout this paper, p'_0 has been set equal to 100 kPa, although other choices are possible), α_i is the wave velocity at the reference stress, and β_i is the so-called Hertz exponent, describing the sensitivity of P- or S-wave velocities on stress.

Other models relate stress dependency to crack closure, providing different expressions from equation 1 (e.g., Katsuki et al., 2014), also foreseeing increase of velocity (stiffness) with loading (see Appendix A for application of the Katsuki et al. [2014] model to one of the case studies of this paper).

Although the role of effective stress on wave velocity is given by relationship 1, the role of porosity and of structure is implicitly included in the two parameters α_i and β_i, whose meaning is discussed in Santamarina et al. (2001). Parameter α_i depends on the elastic properties of the rock grains (e.g., shear modulus G_g and the Poisson's ratio ν_g), on porosity, and on other factors related to structure (particles coordination number, contact behavior, and the presence/type of cement). The type of contact between the particles (e.g., contact area and friction) controls the value of the β_i parameter, which, for the theoretical case of uncemented spherical grains, is equal to $\beta = 1/6$. Experimental data (Santamarina et al., 2001; Cha et al., 2009) show decreasing values of β_i for increasing values of α_i: a volume of rock with high stiffness at the reference stress (high value of α_i) is less sensitive to an increase in stress (i.e., it has a low value of β_i) than another volume of rock with a lower reference stiffness (low value of α_i but high value of β_i). As pointed out by Berge et al. (1993), "Effective elastic properties of composites depend on constituent elastic constants, volume fractions, and spatial arrangement (microstructure)." Parameter α_i can be further interpreted as the product of a constant A_i, related to the stiffness of the solid constituent and a function $F_i(\phi)$, dependent on porosity ϕ at reference pressure and on structure:

$$\alpha_i = A_i F_i(\phi). \quad (2)$$

Some literature expressions for $F_i(\phi)$ are reported by Mitchell and Soga (2005). For materials of low to moderately low porosities, the function $F_i(\phi)$ should comply with the following basic requirements: first, A_i should be constant in geomaterials with the same mineralogy; second, it is convenient to assume that $F_i(\phi)$ tends to unity when the porosity tends to zero (in this case, it profitably follows that A_i represents the velocity of the elastic wave in the rock mineral at the reference effective stress). A phenomenological exponential function allows both prescriptions to be respected:

$$F_i(\phi) = e^{-c_i\phi}, \quad (3)$$

where c_i is a fitting parameter, which depends on the structure of the material. Different c_i values are associated with different structures: if the structure of a population of samples changes, the velocity at a given porosity and reference conditions changes consequently, and this is reflected by different c_i values. Several other equations have been proposed in the literature to take into account the effect of porosity and structure on wave velocity at reference stress (see Mavko et al., 2009). Although these literature expressions ultimately make it possible to guess the type of structure/cementation (Avseth et al., 2010), henceforth equation 3 will be used because of its simplicity. Equation 3, calibrated on laboratory data, is used in the following examples to reflect the structural conditions of samples from the studied rock formations. Figure 1 shows an example of the fitting of experimental laboratory data from the third case history of the present study.

The following steps are needed to provide the structural characterization of a data set of specimens from a homogeneous rock formation (phase 1 in Figure 2):

- Step 1: for each specimen, parameters α_i and β_i of equation 1 are obtained through regression of results of laboratory tests, in which elastic-wave velocities are measured under increasing isotropic load.
- Step 2: the $\beta_i = \beta(\alpha_i)$ relationship is obtained for the data set.
- Step 3: a regression of the values of α_i as a function of porosity (equations 2 and 3) allows parameter c_i to be determined.

Step 3 requires the velocity of the elastic waves in the solid phase A_i to be known. For monomineral rocks, the coefficient A_i can be assumed equal to available literature velocities for the solid constituent. Alternatively, for rocks composed by a mixture of minerals, the coefficient A_i can be assumed as one of the following values: (1) an average velocity (e.g., Hill's average), assuming literature data for wave velocities of each constituent, if the mineralogical composition of rock is available, (2) the wave velocity measured by wellbore sonic logs at negligible porosities or by laboratory ultrasonic measurements

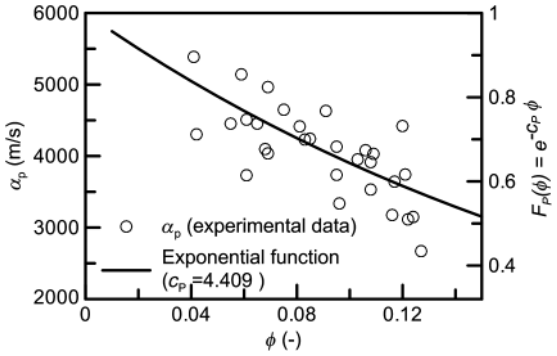

Figure 1. Relationship α_P-ϕ and porosity homogenization function $F(\phi)$ for the laboratory data set of a carbonatic rock.

Step	Description	Equation
	Phase 0 - Preliminary step	
0	"Fluid substitution" is applied to refer laboratory and logging data to the same saturation conditions (e.g., dry conditions if applicability of Gassmann equation is proved; otherwise, strictly use data from dry tests and fluid substitute to in situ conditions)	$K_{sk} = \frac{\left(\frac{\phi}{K_{fl}} + \frac{1-\phi}{K_g}\right)K_{mix} - 1}{\frac{\phi}{K_{fl}} - \frac{1+\phi}{K_g} + \frac{K_{mix}}{K_g^2}}$
	Phase 1 - On the laboratory acoustic measurements	
I	α_i and β_i parameters are evaluated on each sample	$V_i = \alpha_i \left(\frac{p'}{p'_0}\right)^{\beta_i}$
II	A linear regression of α_i and β_i parameters on different samples is used to define α-β relationship	$\beta_i = \beta_i(\alpha_i)$
III	Considering rock constituents minerals parameters and the porosity of each sample, the $F_i(\phi)$ relationship is interpolated with an exponential function	$\frac{\alpha_i}{A_i} = F_i(\phi) \quad F_i(\phi) = e^{-c_i\phi}$
	Phase 2 - On log measurements	
IV	Isotropic effective stress at depth is required	$p'_z = p'(z)$
V	To take into account the effect of stress on porosity, porosity measurements from logs are corrected, and referred to the reference isotropic stress. This allows determining a log of porosity along the well at reference stress. For practical purposes this correction can be omitted if the rock is very stiff and porosity variations from reference to in situ stress are negligible.	ϕ^{log}
VI	$\alpha_i^{pseudo}(z)$ values at depth are evaluated using porosity logs	$\alpha_i^{pseudo} = A_i F_i\left(\phi^{log}\right)$
VII	$\alpha_i^{well}(z)$ is obtained minimizing the difference between pseudo velocity (Equation 1) and velocity logs (with a given stress p'$_z$)	$\left(V_i^{log} - \alpha_i^{well}\left(\frac{p'_z}{p_0}\right)^{\beta_i^{well}}\right)^2 = min$
	Phase 3	
VIII	The structural index ratio is defined to assess sample representativeness. It might be used also to correct velocity logs.	$SI(z) = \alpha^{well} / \alpha^{pseudo}$

Figure 2. Main steps of the methodology used in this study.

performed on very low porosity samples, and (3) a value extrapolated from the regression function between α_i and porosity ϕ, imposing the condition $F_i(\phi) = 1$, for $\phi = 0$.

Fluid effects on wave propagation

Because the fluid saturating the pore space influences the wave propagation in the porous medium, it is necessary to assure that laboratory and well-log data refer to the same saturation conditions. Hence, it is preliminary necessary to account for the dependence of the seismic velocities on the pore fluid (Figure 2 — phase 0).

In fluid-saturated rocks, wave velocities increase with frequency owing to the fluid-solid interaction (Biot, 1956a, 1956b; O'Connell and Budiansky, 1974; Mavko and Nur, 1979; Murphy et al., 1986; Dvorkin and Nur, 1993; Dvorkin et al., 1994). Two main mechanisms have been identified: (1) the Biot one, in which the fluid is forced to participate in the solid motion by viscous friction and inertia and (2) the squirt-flow mechanism, in which the fluid is squeezed out of thin pores deformed by a passing wave. The dispersion effect caused by the squirt flow (local flow) is usually comparable with or larger than the effect predicted by the Biot theory alone (global flow).

The global and local flow mechanisms have been incorporated into a single model (Dvorkin and Nur, 1993; Dvorkin et al., 1994). Although this complete model allows a comprehensive interpretation of acoustic data, it requires a microstructural parameter (e.g., the squirt-flow length) that is not easily estimated (Diallo et al., 2003).

The simplest and most widely used model to calculate elastic waves velocity changes resulting from different fluid saturations is the Gassmann's fluid substitution formula (Gassmann, 1951). This model is based on Biot's poroelasticity theory (global flow), and its application requires several assumptions to be respected: the rock (matrix and frame) is macroscopically homogeneous and isotropic; the pores are interconnected or communicating and in pressure equilibrium; the pores are filled with a frictionless fluid (liquid, gas, or mixture); the rock-fluid system under study is closed (undrained conditions); there is no chemical interaction between fluids and rock frame (shear modulus remains constant); and the influence of squirting is negligible. Some of these assumptions may not be valid for a specific data set, depending on rock properties, wave frequency used in testing, viscosity, and compressibility of the fluid. In particular, the low-frequency formulation of Biot's theory (Biot, 1956a) can be used for operating frequencies below the following threshold:

$$f_c = \frac{\phi \eta_{fl}}{2\pi \rho_{fl} k}, \tag{4}$$

where η_{fl} and ρ_{fl} are viscosity and density of the pore fluid, respectively, and k is the rock permeability.

Therefore, to refer laboratory and log data to the same saturation conditions, it is possible to operate in two ways (Figure 2 — phase 0): (1) use only dry laboratory measurements of wave propagation and (2) test the validity of Gassmann's theory comparing the results of laboratory ultrasonic velocity measurements at different saturation conditions (Grochau and Gurevich, 2009; Rasolofosaon and Zinszner, 2012).

In the first case, dry measurements are used to mitigate the effects associated with the dispersion caused by fluid-solid interaction (Grochau and Gurevich, 2008), so Gassmann's equation can be applied on dry ultrasonic measurements to refer laboratory data to the reservoir saturation conditions. Other dispersion phenomena may still affect the wave velocity measurements (e.g., scattering and matrix anelasticity); however, these phenomena can be usually assumed negligible with respect to effects due to dispersion from fluid-solid interaction. Therefore, the velocities computed from dry measurements using Gassmann's equation can be considered as measured in the low-frequency (quasistatic) limit (Grochau and Gurevich, 2008). In the other case, if the applicability of Gassmann's equation on ultrasonic laboratory data is verified (e.g., as in Appendix B), it is possible to apply the fluid substitution to log data as well because testing frequencies in the field are typically lower than those in the lab. The laboratory and log data can be therefore transformed into equivalent values at dry conditions.

Comparing laboratory and log velocities: The structural index

Processing of an ultrasonic laboratory data set allows the definition of the $\beta_i(\alpha_i)$ and $F_i(\phi)$ relationships (see the previous section "Fluid effects on wave propagation" and Figure 2) for samples proceeding from a formation of interest.

Such a characterization can be used to evaluate an index for the assessment of structural integrity. This index relies on referring laboratory and log data to common reference conditions, and it allows the quantitative assessment of structure differences between the samples of the data set and the in situ rock formation. The in situ isotropic effective stress p'_z, porosity, and sonic waves velocity logs are needed for this aim. The main steps for derivation of the index are summarized in phases 2 and 3 of Figure 2 and commented in this section.

Equation 2 shows the dependency of parameter α_i on mineralogy, porosity at reference stress (100 kPa in this study), and structure. The last two variables are merged together in the porosity homogenization factor $F_i(\phi)$. At a given porosity at reference pressure, an exponential relationship between α_i and structure exists, which is expressed by exponent c_i in equation 3. We call α_i^{pseudo} the value expected for α_i, according to laboratory characterization. The parameter α_i^{pseudo} projects the structure of the sample data set along the well. A log of α_i^{pseudo} is obtained by introducing the porosity log $\phi^{\log}$ and the experimental value of c_i in equation 3, and then multiplying the result by the velocity of the solid A_i (Figure 2, phase 2, steps IV, V, and VI). The parameters are maintained constant throughout the considered depth interval, along which sufficient mineral homogeneity shall exist. Note that the porosity log shall be corrected to have porosity at the reference stress: this can be done using static bulk moduli obtained in the laboratory.

Equation 1 shows the relationship between stress α_i and $\beta_i(\alpha_i)$. If the isotropic stress in the formation p'_z is known, local values of α_i for the rock formation at its original undisturbed state (α_i^{well}) are estimated along the well by means of an optimization procedure (Figure 2, phase 2, step VII). This procedure relies on the $\beta_i = \beta(\alpha_i)$ relationship obtained in the laboratory. By introducing p'_z in equation 1, it is possible to estimate the couple of α_i and β_i parameters minimizing the scatter between a predicted velocity $\alpha_i(p'_z/p'_0)^{\beta_i}$ and the velocity $V_i^{\log}$ measured with sonic logging. The sequence of α_i values obtained this way (namely α_i^{well}) represents the estimation of α_i within the formation and it is representative of the actual structure.

The *structural index* (*SI*) can be defined at each depth as

$$SI = \alpha_i^{\text{well}} / \alpha_i^{\text{pseudo}}, \tag{5}$$

and it represents the ratio of the effects of the undisturbed structure of the formation to the effects of the average structure of the population of laboratory samples on wave velocities. Mechanical processes (e.g., coring or tectonic events) may destroy the structural connections developed during previous geologic history changing the relationship between α_i and ϕ. The *SI* allows evaluating the difference between the local and the laboratory data set $\alpha - \phi$ relationships.

When *SI* is equal to 1, the sample data set and the rock formation have the same structure, and laboratory tests are fully representative of the behavior of the rock formation. In other words, at the same given porosity, reference pressure and saturation conditions, the rock formation and the samples will have the same elastic-wave velocity. Two other cases are possible:

$SI = \alpha_i^{\text{well}} / \alpha_i^{\text{pseudo}} > 1$: the wave velocity of the formation, measured by sonic loggers and extrapolated to reference conditions, is higher than the one predicted, for the local porosity, on the basis of the characterization made on laboratory samples. Therefore, this case suggests that the structure of the formation has been partially destroyed during coring and that sample data set underwent some damage.

$SI = \alpha_i^{\text{well}} / \alpha_i^{\text{pseudo}} < 1$: the wave velocity of the formation, measured by sonic loggers and extrapolated to reference conditions, is lower than the one predicted, for the local porosity, on the basis of the characterization made on laboratory samples. This case suggests that fractures not represented in the samples are actually present in the formation.

An alternative way to assess differences between the structure of the rock samples and that of the rock is also suggested. Once α_i^{pseudo} has been evaluated at each depth, by applying equation 1, a pseudolog of the expected elastic-wave velocity can be derived. Differences between measured velocities of sonic logs and velocities of this pseudolog are due to differences between the structure of the rock in situ and in the laboratory.

Nevertheless, the proposed *SI* has the following advantages: first because higher values of β_i correspond to lower values of α_i, the increase of the elastic-wave velocity with stress is higher in damaged samples than in the supposedly undisturbed formation. Thus, at in situ stresses, the impact of structure on wave velocity is somehow smeared out, whereas it is more evident at low stresses, such as the reference stress. Second, the use of a reference condition allows the assessment of the actual damage and megastructural effects occurring at different depths of the same well (or in different wells of the same field). The same difference in velocity between the pseudolog and the sonic log at different depths does not indicate identical structural damage if the stress state is different, such as it could be along wells and formations extending over large depths. Finally, when populating geomechanical models at large scales, the *SI* index provides support to extrapolate information from undisturbed samples.

A modified α_i^{pseudo} can be defined using core porosity, if available, in place of log porosity in the proposed formulation. Its use in equation 5 leads to a different index, that we shall call the *damage index* (DI), accounting also for the effects of porosity changes at reference pressure induced by coring. More details on this index and its implications are provided in Appendix C.

GEOMECHANICAL CHARACTERIZATION AT WELL SCALE

Laboratory tests (e.g., triaxial test) can be used to characterize the formation of interest on a wide stress/strain interval, whereas only dynamic (small strain) moduli are measured by sonic logs.

If the *SI* is close to one (i.e., lab samples have on average the same structure of the in situ formation), the information from the lab and sonic log can be integrated to build a comprehensive geomechanical model. In this case, the stress-strain relationship measured in laboratory tests (e.g., triaxial tests) is used to experimentally evaluate the decrease of the secant shear modulus as a function of strain. The experimental data are interpreted through an analytical expression (e.g., Ramberg and Osgood, 1943; Duncan and Chang, 1970; Puzrin and Burland, 1996). The same expression is used along the well to estimate the shear modulus at any strain level, provided that the initial (small strain modulus) is evaluated through

$$G_0 = \rho V_S^2, \tag{6}$$

with V_S measured by sonic logs.

In the present study, the law of Ramberg and Osgood (1943) was used because it produces a very good fitting with the case histories reported in the next section, "Application to experimental data sets."

An analogous procedure can be applied to estimate the bulk modulus. The ratio K_{0us}/K_{tg} (where K_{0us} is the bulk modulus at small strain levels from ultrasonic measurements and K_{tg} is the tangent bulk modulus) is evaluated at increasing stress levels during laboratory tests. An experimental relationship is thus determined between the dynamic and the static moduli through which log data can be calibrated. The small strain modulus K_{0us} is determined as

$$K_{0us} = \rho\left(V_P^2 - \frac{4}{3} V_S^2\right), \tag{7}$$

where V_P and V_S are measured by ultrasonic tests or sonic logs.

APPLICATION TO EXPERIMENTAL DATA SETS

Application to three data sets, one related to synthetic rock samples and two derived from field cases, is discussed in the following. In the first two cases, in which data are obtained from the literature, only the evaluation of the *SI* to define the representativeness of samples with respect to the rock formation is derived. In the last case, in which a more complete data set is available, a further analysis aimed at characterizing the geomechanical stratigraphy is also performed.

Application 1: Quantification of coring damage on synthetic rock samples

Experimental data reported in Holt et al. (2000) offer an interesting benchmark to validate the proposed procedure. Indeed, their tests were specifically designed to reproduce the effect of core damage induced by sampling on the mechanical behavior of rocks, so

that material parameters measured in virgin condition could be compared with those measured on cored samples. Samples of synthetic rock were manufactured mixing sand grains with sodium silicate solution into a wet slurry. The wet sand pack was loaded in a triaxial cell to a high confinement stress, representing the in situ stress state of a target reservoir (30 MPa vertical and 15 MPa horizontal stress).

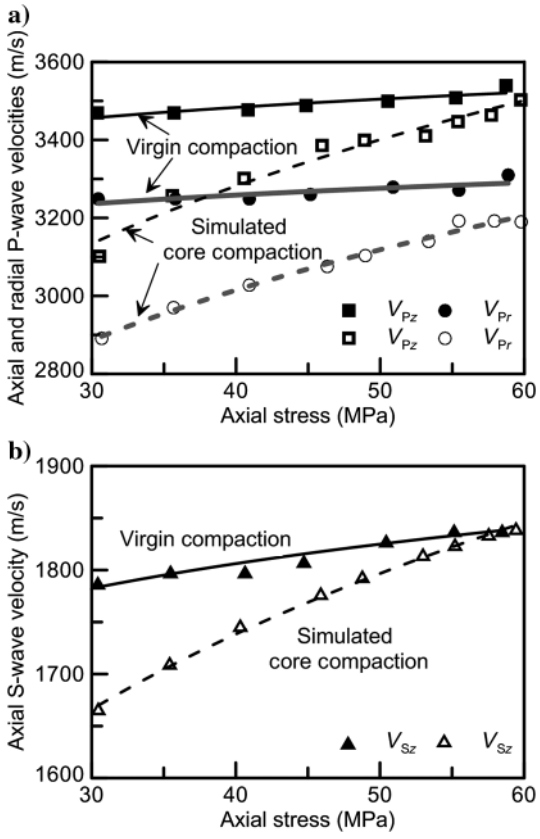

Figure 3. Laboratory axial and radial P-wave velocities (a) and axial S-wave velocities (b) versus axial stress during uniaxial compaction tests of virgin compaction (filled symbols) and simulated core compaction (unfilled symbol) (data are from Holt et al., 2000). Fitting curves predicted by equation 1 are reported as solid and dashed lines for virgin compaction and simulated core compaction, respectively.

Table 1. Estimated parameters for the Holt et al. (2000) data.

	P-wave		S-wave
	Axial	Radial	Axial
α virgin compaction (m/s)	2959	2823	1369
α simulated core compaction (m/s)	1260	1218	717
$SI = \alpha_{virgin}/\alpha_{core}$	2.34	2.31	1.91
β (virgin compaction)	0.0273	0.0240	0.0462
β (simulated core compaction)	0.1598	0.1513	0.1477

CO_2 gas was then injected into the samples, leading to rapid precipitation of amorphous silica at grain contacts. Damage effects due to coring procedure were simulated by unloading the samples. The mechanical behavior of the altered samples was studied reloading them back to the previous stress state. The stress dependence of P- and S-wave velocities was measured in the cemented state, before unloading (virgin compaction), and after core damage (*simulated core compaction*).

Figure 3 reports the experimental data of P (3a) and S (3b)-wave velocities on samples in the virgin compaction condition and in simulated core compaction. The velocities were measured at increasing axial stress in oedometer conditions. The P-wave velocities were recorded along the sample axis and across the sample diameter, whereas the S-wave velocities were only measured along the sample axis. These experimental data can be fitted with equation 1 to obtain the values of α_i and β_i for each type of wave and for each sample (Table 1). As expected, destructuration induced by coring causes a decrease of α_i and a corresponding increase of β_i (Figure 4). For this data set, the α_i values of virgin compaction (α_i^{virgin}) can be assumed as α_i^{well} and the *SI* can be calculated as $\alpha_i^{virgin}/\alpha_i^{core}$. Values of *SI* in Table 1 (all above 1) quantify the effect of coring on structure.

Although Holt et al. (2000) report ratios between the virgin and cored states oedometer modulus ranging between 2 and 3, the *SI* ranges between 1.91 (S-waves) and 2.34 (axial P-waves). Note that *SI* is related to the velocity extrapolated at a stress of 100 kPa. Because velocity is proportional to the square root of the modulus, these results suggest that effects of coring are more evident at low stresses and small strains.

P-wave velocities were recorded along the sample axis and across the sample diameter; therefore, two SI_P, one for each direction, were evaluated. This would allow us to take into account anisotropy effects (velocities varying with the direction of propagation) if similar in situ measurements are available. In situ anisotropy can be obtained for example by means of the multioffset multiazimuthal vertical seismic profiling (Okaya et al., 2004; Asgharzadeh et al., 2013) or by the S-wave splitting analysis (Crampin, 1985; Savage, 1999; Peng and Ben-Zion, 2004).

Application 2: Sandstone reservoir

A second case history refers to a well drilled in a quartz arenite sandstone (Mantilla, 2002) proceeding from Colombia (Apiay-Guatiquía oil field). The set of available geophysical measurements

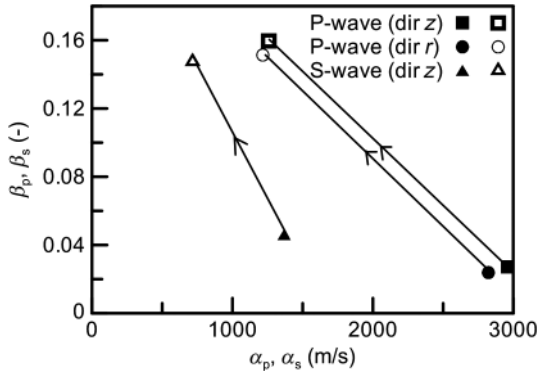

Figure 4. Case history 1: effect of sample destructuration on α_i and β_i.

consists of the following logs: gamma-ray, spontaneous potential, neutron porosity, bulk density, P-wave slowness, caliper, shallow, intermediate, and deep resistivities. Gamma-ray logs and petrographic analysis in Mantilla (2002) have evidenced a relatively uniform mineralogy, excluding depths ranging between 3245 and 3260 m and a thin layer at a depth of approximately 3310 m, where shale components are abundant. Because laboratory characterization is available only for sandstone samples, it was not possible to evaluate the *SI* in these intervals. At other depths, the presence of shale is mostly negligible because the gamma ray only shows isolated peaks. Moreover, thin-section analyses provided by Mantilla (2002) show relatively uniform mineralogy also for gamma-ray anomalies ranging from 20 up to 100 API.

Laboratory ultrasonic P- and S-wave velocities under increasing isotropic stress are also available for several cores along the well. The dependence of P and S velocities on stress, and its interpretation in terms of equation 1, is reported in Figure 5 (see also Table 2 providing values of associated α_i and β_i parameters).

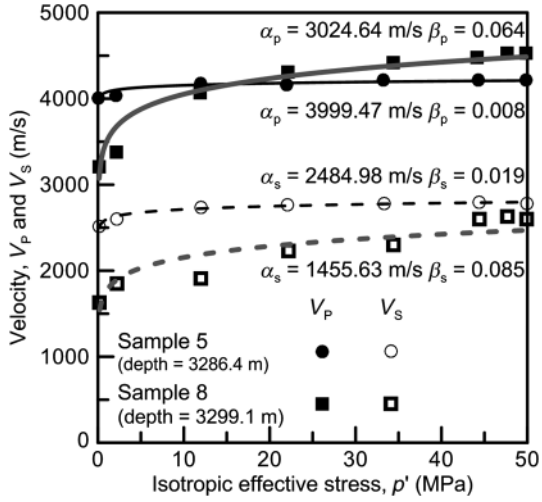

Figure 5. Case history 2: determination of the α_i and β_i parameters through regression of ultrasonic laboratory measurements on two representative samples (data from Mantilla, 2002).

Total stress gradients (increase of total stress per unit increase of depth) are also indicated in Mantilla (2002): 22.62 kPa/m for the vertical stress, 21.26 and 13.80 kPa/m for the maximum and minimum horizontal stress, respectively, with a mean stress gradient of 19.23 kPa/m. Using this information and the laboratory experimental data, the α_i-β_i relationships (Figure 6), the $F_p(\phi)$ function (Table 2), and the *SI* (Figure 7, where the main original logs of this well are also provided) were evaluated. The porosity log was not corrected for effects of unloading from the in situ to the reference stress because Mantilla (2002) reports negligible porosity changes

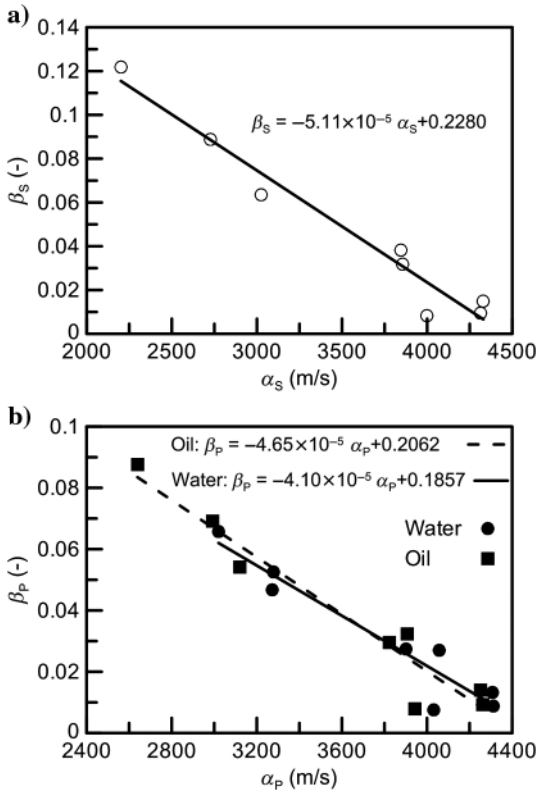

Figure 6. Relationship α-β for P-wave for laboratory samples from well 3 of the Apiay-Guatiquía field (data from Mantilla, 2002).

Table 2. Estimated parameters for the Apiay-Guatiquía field, well 3 (data from Mantilla, 2002).

Sample	Depth (m)	ϕ (%)	α_P (m/s)	β_P (–)	α_S (m/s)	β_S (–)
3	3261.5	16.79	3846.49	0.038	2899.91	0.015
4	3276.4	18.38	3855.95	0.032	2246.95	0.048
5	3286.4	21.69	3999.47	0.008	2484.98	0.019
6	3287.1	18.51	4329.97	0.015	2665.49	0.024
7	3288.6	15.79	2200.84	0.122	2080.53	0.044
8	3299.1	16.69	3024.64	0.064	1455.63	0.085
9	3300.8	15.60	4314.51	0.010	2555.64	0.021
10	3304.0	14.58	2726.67	0.089	1744.28	0.051

The A_P = 6050 m/s, A_S = 4090 m/s (from P- and S-wave velocities in quartz, Mavko et al., 2009).

The c_P exponent of the function $F_P(\phi) = e^{-c_P \cdot \phi}$, obtained through of α_P/A_P versus ϕ, is equal to 3.124.

due to compression (changes between -1.0×10^{-4} and -8.9×10^{-3} when loading from $p' = 0$ to 45 MPa). In this exercise, it was not possible to exclude frequency dispersion effects due to squirt mechanisms. Velocities obtained in the laboratory on samples in dry or residual saturation conditions were then corrected through Gassmann fluid substitution, accounting for the effect of stiffness and density of oil ($\rho_{oil} = 900$ kg/m^3 and $K_{oil} = 1.43$ GPa) and of brine ($\rho_w = 1055$ kg/m^3 and $K_w = 3.013$ GPa), and thus allowing comparison of the characterization with sonic-log data.

Along the well, many portions having an *SI* well below one are evidenced, so that at reference conditions, samples shall have higher velocities than the formation, suggesting that fractures are diffusely present. In particular, there are three depth intervals, where *SI* assumes very low values. In the same zones, shallow, intermediate and deep resistivity logs show a reduction of resistivity (Figure 7), which is accepted as a consolidated evidence of the presence of fractures (see, e.g., Ellis and Singer, 2008).

Application 3: Carbonate reservoir

A third case history is related to the characterization of a carbonate rock within an oil reservoir (whose location is omitted because of industrial interest). The following logs had been performed in the well: gamma-ray, bulk density, P- and S-waves slowness, resistivity, and neutron porosity. Laboratory tests, carried out on specimens obtained from cores of the same well, included porosity measure-

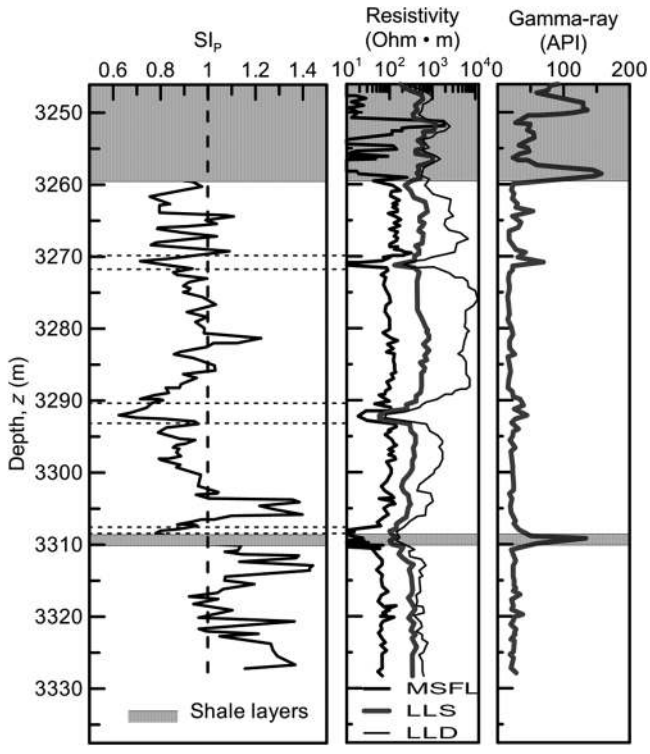

Figure 7. P-wave $SI = \alpha^{well}/\alpha^{pseudo}$ log for well 3 of the Apiay-Guatiquía field (left) compared with shallow (MSFL, microspherical focused log), intermediate (LLS, shallow laterolog) and deep (LLD, deep laterolog) resistivity logs (center), and gamma-ray log (right). Based on data from Mantilla (2002). Shadow zones represent shale layers individuated on the base of petrographic analysis.

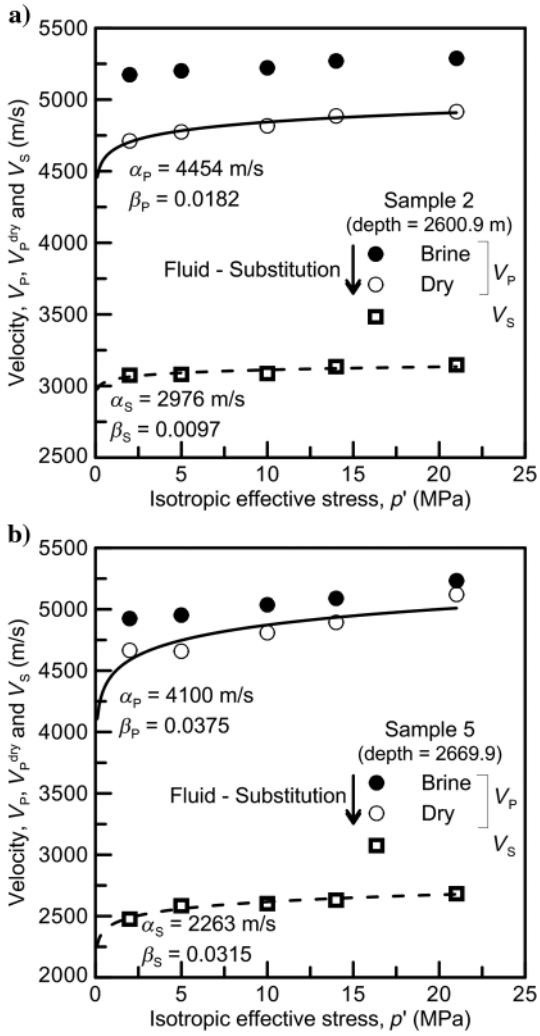

Figure 8. Case history 3: application of Gassmann's fluid substitution and determination of the α_i and β_i parameters for two laboratory samples.

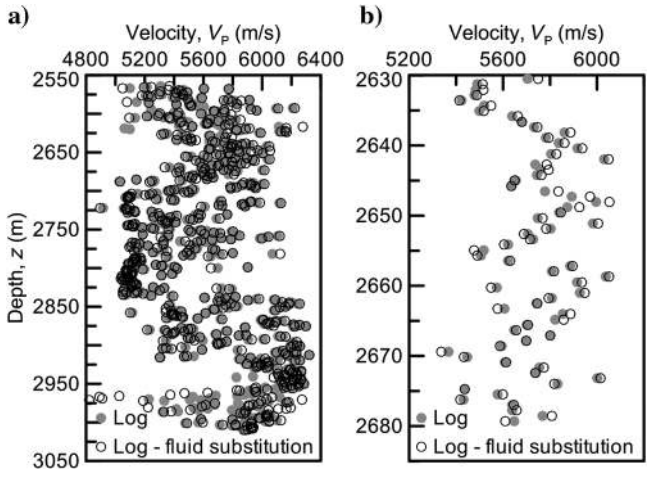

Figure 9. Case history 3: (a) application of Gassmann's fluid substitution to P-wave acoustic logs on a representative depth interval. (b) Magnification of a portion of the same graph.

ments, uniaxial tests, triaxial tests, and ultrasonic wave velocity measurements performed at increasing isotropic stress. Ultrasonic measurements were carried out on dry, brine-saturated, and oil-saturated specimens.

Because sonic logs and ultrasonic tests were performed at different saturations, Gassmann's fluid substitution procedure was applied to refer all measures to dry conditions. The validity of Gassmann's equation was tested experimentally by comparing ultrasonic laboratory tests performed at different saturations (see Appendix B). The effect of fluid substitution on laboratory and in situ wave velocities is shown, respectively, in Figures 8 and 9. Figure 8 shows V_P velocities as measured on brine saturated specimens and as estimated, through fluid substitution, at dry conditions. Figure 9 analyzes a selected depth interval of the well, and compares the original V_P log with the V_P log at dry conditions as obtained through fluid substitution. Actual local saturation degrees of water and oil, of known physical properties, were used to operate fluid substitution in this latter case.

The parameters α_i and β_i of each sample were determined through a mean-square regression of V_P and V_S data versus isotropic stress, based on equation 1. An example of the obtained fitting is shown in Figure 8, whereas α_i and β_i values for all samples are reported in Table 3. Two relationships $\beta_i = \beta(\alpha_i)$ valid for the data set were derived: one for P-waves (Figure 10a) and the second for S-waves (Figure 10b).

X-ray analyses have shown that calcite is the only mineral constituting the grains, so values of the A_i parameters in equation 2 can be assumed from the literature: $A_P = 6264$ m/s and $A_S = 3426$ m/s (after Mavko et al., 2009) were considered. Interestingly, these values of A_P and A_S are in agreement with sonic velocities of P- and S-waves measured by logs in intervals of very low porosities (Figure 11). The $F_i(\phi)$ relationships (equation 3) were then determined by deriving

Table 3. Values of α_i and β_i parameters for all the samples of case history 3.

	Sample	Depth (m)	α_P (m/s)	β_P (–)	α_S (m/s)	β_S (–)
Brine with fluid substitution	2	2600.9	4454.75	0.018	2976.86	0.009
	5	2669.9	4100.34	0.037	2263.35	0.031
	7	2685.4	4032.60	0.047	1978.51	0.042
	8	2688.1	2671.48	0.117	2107.34	0.042
	9	2699.8	3337.92	0.065	2217.61	0.041
	10	2702.7	4243.41	0.021	2239.44	0.030
	11	2704.5	4135.26	0.066	1990.26	0.075
	13	2734.9	4649.86	0.031	2536.73	0.025
	14	2736.2	5145.92	0.018	2760.60	0.013
	15	2738.7	4632.23	0.026	2358.75	0.038
	16	2751.1	4968.54	0.030	2751.59	0.020
	17	2755.1	4304.60	0.043	2836.03	0.016
	18	2794.5	3957.59	0.034	2474.74	0.017
	19	2800.8	4454.91	0.032	2684.70	0.031
	21	2828.6	4417.22	0.035	2660.64	0.010
	22	2834.0	3151.26	0.078	2000.77	0.051
	23	2849.0	3918.48	0.049	2403.05	0.014
	24	2852.2	4421.03	0.023	2327.96	0.031
	25	2915.8	4232.68	0.043	2511.48	0.026
	26	2917.2	5389.78	0.017	2832.62	0.006
Dry	1	2589.0	4509.07	0.040	2546.21	0.032
	27	2596.3	4080.03	0.052	2305.82	0.052
	28	2687.4	3641.53	0.048	2069.53	0.048
	29	2708.8	3744.70	0.053	2056.66	0.053
	30	2711.6	3731.84	0.057	2220.16	0.050
	12	2721.9	3115.35	0.074	1978.16	0.071
	31	2745.4	3737.61	0.051	2075.77	0.051
	32	2806.1	3532.24	0.055	2029.17	0.055
	20	2809.0	3175.17	0.078	1911.08	0.073
	33	2851.9	4037.07	0.054	2193.43	0.054

the exponent c_i with a mean-square regression of the data (Figure 12). The obtained $\beta_i(\alpha_i)$ and $F_i(\phi)$ relationships were used to generate P and S pseudovelocity logs, which can be compared with the sonic logs (Figure 13). To increase readability, Figure 13b and 13d provides the difference between the velocities of the fluid substituted logs and those predicted by the pseudolog. Log velocities are mostly higher than those predicted by the pseudolog. Note that the pseudolog requires the profile of the effective isotropic stress. For its evaluation, measured fluid pressures were used; the total vertical stress was derived using density logs, the minimum total horizontal stress was obtained from minifrac and leak-off tests, and the maximum horizontal stress was obtained based on inversion of breakout and tensile failure data (see, e.g., Zoback et al., 1985; Della Vecchia et al., 2014). Also in this case, the log porosity was not corrected for stress change effects because the maximum porosity variation induced by isotropic compression from unloaded conditions to 30 MPa (Table 4) was equal to 2.2×10^{-3}.

Finally, the optimization procedure described in the section "Comparing laboratory and log velocities," based on the α-β relationship, on equation 1 and on the stress profile, was applied to generate the profile of $\alpha_i^{\text{well}}(z)$, and the *SI* (Figure 14). The values of *SI* are slightly above 1; in some localized zones of the well, however, a strong decrease in the index with depth (particularly noticeable in the P-waves plot) could suggest that the reservoir presents alterations possibly related to the presence of fractures not represented in the samples.

However, *SI* values derived for P- and S-waves are actually quite close to one, thus indicating that the samples can be considered representative of the reservoir formation. As a consequence, the geomechanical model can be derived following the procedure described previously. Along the formation, a profile of the secant shear modulus can be obtained integrating information from the deviatoric phase of triaxial laboratory tests, whereas data from the isotropic consolidation phase can be used to integrate information on the bulk stiffness.

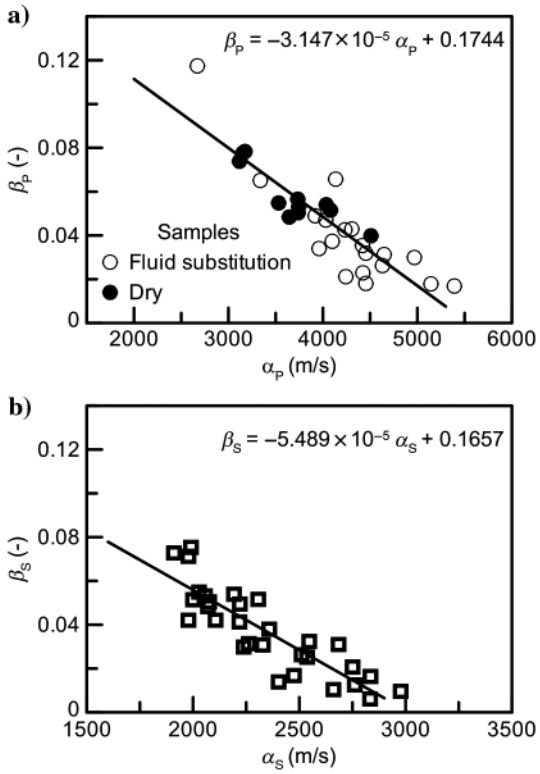

Figure 10. Case history 3: α-β relationship for (a) P-wave and (b) S-wave from laboratory data.

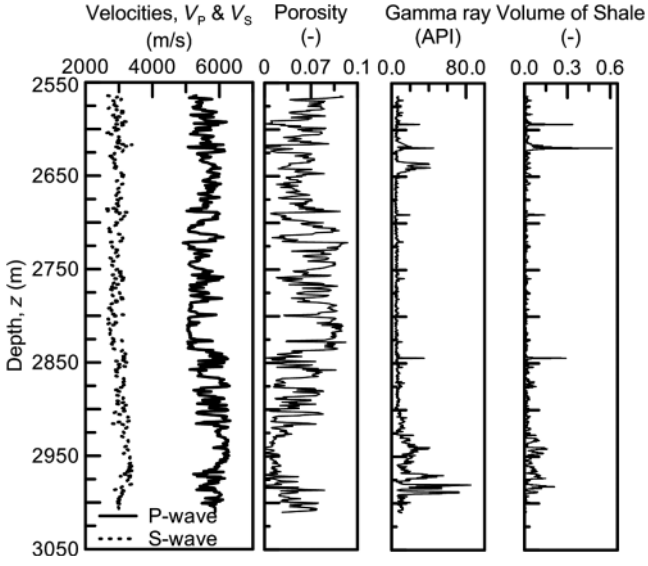

Figure 11. Case history 3: P- and S-wave acoustic logs, porosity, gamma ray, and volume of shale logs.

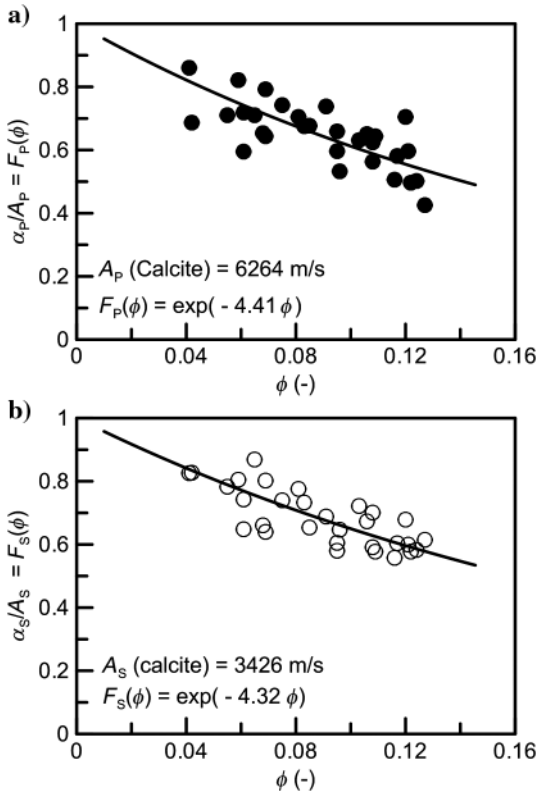

Figure 12. Case history 3: $F(\phi)$ relationship for (a) P-wave and (b) S-wave from laboratory data.

Strictly speaking, this would be applicable if ultrasonic measurements were performed during the triaxial tests. However, the methodology can also be adopted when ultrasonic and triaxial tests are available on separate samples from the data set, as in this case history.

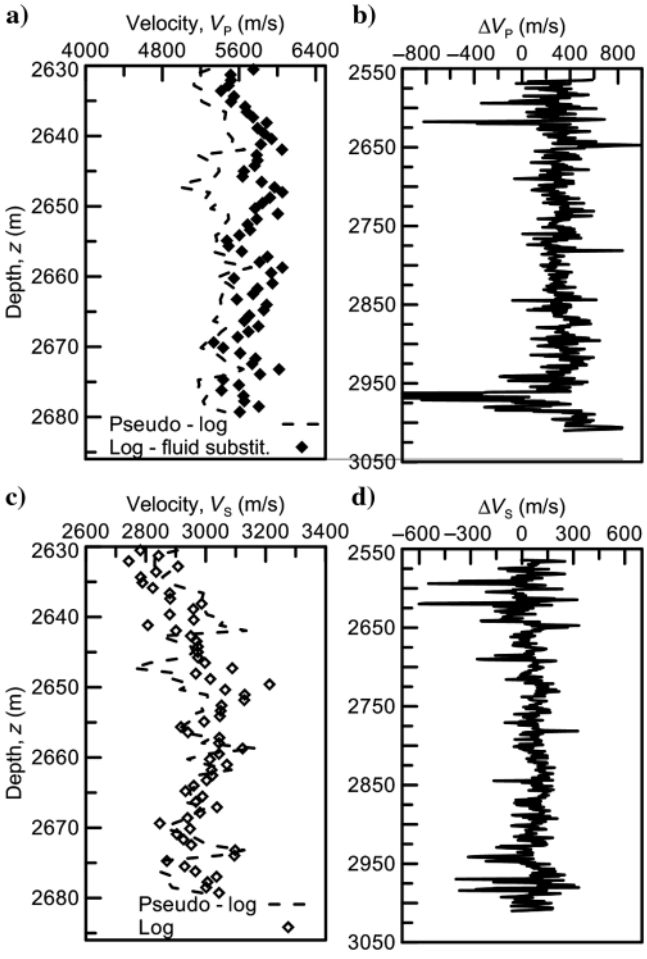

Figure 13. Case history 3: Comparison between acoustic velocity logs and pseudo velocity logs for (a) P-wave and (c) S-wave along a selected depth range of the well. (b and d) Difference between measured (after fluid substitution) velocities and those predicted by pseudologs.

The secant shear modulus decay as a function of the applied strain, is shown in Figure 15a for a sample of the case history. Figure 15b reports the stress-strain curve for the same sample. The plots show the experimental data derived from the deviatoric phase of the triaxial test M7 (solid lines), performed on a dry sample, together with the fit of the experimental data obtained using the Ramberg and Osgood law (dotted lines):

$$q = G_0 \frac{3\varepsilon_s}{1 + \alpha_0 \left| \frac{q}{q_{\max}} \right|^{r-1}}, \tag{8}$$

where q and $q_{\max}$ are the current and peak deviatoric stress, ε_s is the deviatoric strain, G_0 is the shear modulus at small strains, and α_0 and r are fitting parameters. In the dotted-line model, G_0 is evaluated on the basis of triaxial data at small strains, whereas in the dashed-line model, G_0 is derived from interpretation of ultrasonic measurements performed on a sample from a similar depth having a comparable porosity ($\phi_{tx} = 9.91\%$ and $\phi_{ultrasonic} = 9.1\%$). The identification of fitting parameters for the formation of interest

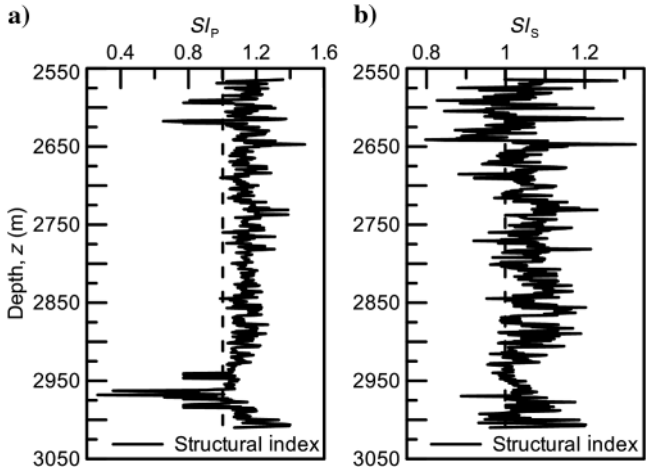

Figure 14. Case history 3: $SI = \alpha^{well}/\alpha^{pseudo}$ versus depth for (a) P-wave and (b) S-wave.

Table 4. Data set of samples used for triaxial testing for the case history 3.

Specimen	Depth (m)	Confining pressure (MPa)	Core porosity (%)	q/q_{max} (at 0.1% strain)
M1	2762.21	0 (unconfined compression)	10.03	—
M2	2845.53	0 (unconfined compression)	5.83	—
M3	2846.05	0 (unconfined compression)	9.12	—
M4	2817.67	10	11.29	0.34
M5	2855.93	10	5.93	0.26
M6	2789.87	10	8.03	0.52
M7	2743.23	30	9.92	0.36
M8	2751.21	30	5.25	0.34
M9	2781.10	30	9.53	0.28

allowed deriving a log for the static shear modulus G, according to the desired strain level by applying equation 8 written as

$$G = \rho V_S^2 \frac{1}{1 + \alpha_0 \left| \frac{q}{q_{max}} \right|^{r-1}}, \quad (9)$$

where the ratio q/q_{max} is relevant for the chosen strain level and V_S is the shear velocity measured with the acoustic log.

The tangent bulk modulus K_{tg} increases with increasing isotropic stress, while the ratio K_{0us}/K_{tg} obtained during the isotropic consolidation phase of triaxial tests decrease as shown in Figure 16a, being K_{0us} the bulk modulus at small strain evaluated on the base of ultrasonic measurements.

Relevant literature shows ratios K_{0us}/K_{tg} close to 1 upon unloading (see, e.g., Fjær, 2009), thus suggesting that K_{0us} is closely related to what, under an elastoplastic frame of interpretation, would be the purely elastic component of the stiffness modulus. The same literature often also shows that along loading paths, in oedometer or isotropic conditions, K_{0us}/K_{tg} has a minimum slightly greater than one at some relatively high stress, whereas it can increase again at even higher stresses. This second aspect could be explained consid-

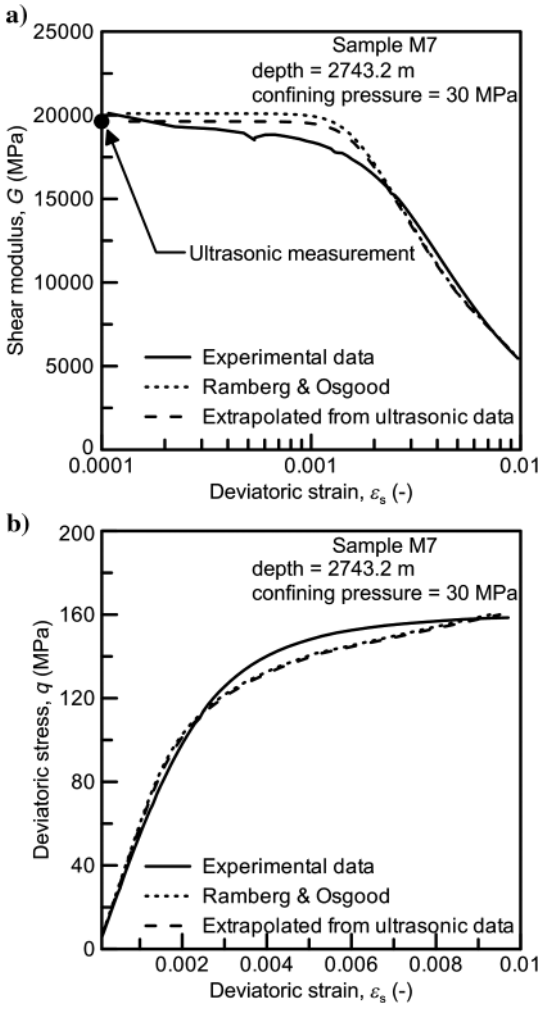

Figure 15. Case history 3: (a) Shear modulus decaying functions and (b) stress-strain curves from experimental data compared with predictions based on the Ramberg and Osgood expression. Predictions done assuming G_0 values from static measurements during triaxial test (dotted line) and from velocity relationships from ultrasonic data (dashed line).

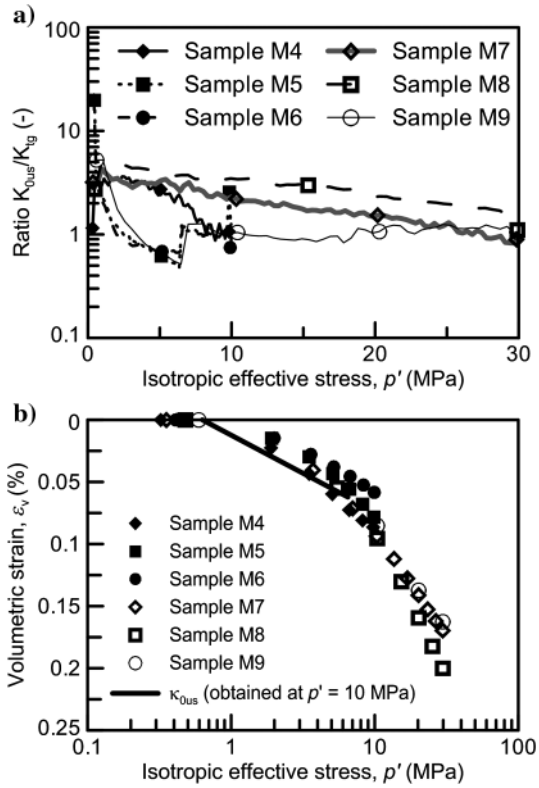

Figure 16. Case history 3: (a) profiles of secant shear stiffness, estimated at a reference strain $\varepsilon_s = 0.1\%$ and (b) of bulk logarithm compliance.

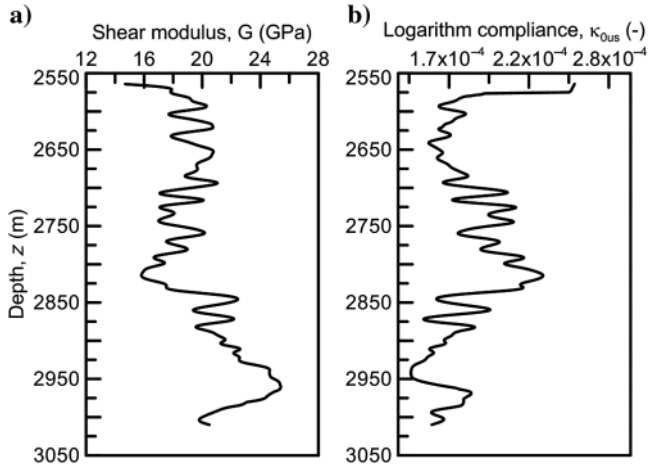

Figure 17. Case history 3: (a) ratio of the bulk modulus at low strains evaluated with ultrasonic tests (K_{0us}) to the tangent bulk modulus from isotropic compression in triaxial tests (K_{tg}) versus isotropic effective stress and (b) isotropic compression curves from experimental data (symbols) and as simulated from logarithm compliance κ_{0us} evaluated through equation 10 (continuous line).

ering that the "static modulus" decreases upon hardening; then minimum values of the K_{0us}/K_{tg} ratio would be obtained upon start of yielding.

Altogether, this suggests the possibility of using the modulus obtained from fluid substituted logs, referred to the proper stress level, to define the elastic stiffness of elastoplastic models. Interestingly, for the present data set, K_{0us}/K_{tg} approaches one upon loading at high stresses of approximately 10 MPa (see Figure 16a). Because geomechanical simulations often rely on elastoplastic models that predict a nonlinear elastic behavior before yielding, this was used to obtain a logarithm compliance κ_{0us}, defined as

$$\kappa_{0us} = \frac{p'}{K_{0us}}, \tag{10}$$

which was estimated at a stress of 10 MPa. Figure 16b shows the agreement between the stress-strain relationship from the triaxial tests and the prediction based on the compliance κ_{0us} from ultrasonic data. A shear modulus log (Figure 17a) and a logarithm compliance log (Figure 17b) were then generated according to equations 9 and 10. In using equation 9, a reference deviatoric strain of 0.1% was considered. In the case of the triaxial tests of Table 4, the reference strain corresponds to a *q/qmax* ratio of 0.35.

CONCLUSIONS

A methodology to evaluate the representativeness of laboratory samples in a quantitative way is proposed, based on joint processing of laboratory tests and wellbore sonic logs. The main objective is to obtain a reliable characterization of the mechanical behavior of the rock formation. Laboratory results have the advantage of investigating a wide strain range and of imposing desired stress paths; however, samples may be not representative of the in situ conditions because damaged and/or not including features (joints and fractures) that could be present in the field. On the contrary, measurements at the well scale (from sonic logs) provide information not biased by coring processes but giving a response limited to the very small strain range. At a given effective stress, saturation and porosity, alterations such as cracks, particle debonding, or fractures induce a decrease of elastic-wave velocities, so velocities measured and predicted at reference conditions ($p'_0 = 100$ kPa, dry rock) can be used to compare the structure and the mechanical properties of the samples with those of the rock formation. Ultrasonic lab tests were integrated with in situ sonic logs to define a structural index, used to quantify the representativeness of the data set of laboratory samples and to guide in using the parameters obtained in the lab (e.g., from triaxial tests) into a reliable geomechanical model for the formation.

By referring to reference conditions, the present methodology has the advantage of providing an index that allows a uniform comparison between samples and formation. Such a uniform comparison could not be achieved with other analyses based on the same physical principles, such as, for instance, projection of results of laboratory seismic data at the in situ conditions.

The proposed methodology has been applied to three case histories. In particular, the last case history shows the potentiality of the method for the characterization of the in situ formation, by extending the local information from the laboratory samples to the scale of interest for engineering applications.

APPENDIX A

COMPARISON OF PREDICTIONS OF STRESS DEPENDENCE OF ELASTIC WAVE VELOCITIES BASED ON A HERTZ-MINDLIN-LIKE MODEL WITH PREDICTIONS BASED ON A CRACK-CLOSURE MODEL

Stress dependency of elastic wave velocities can be modeled ascribing stiffness increase to closure of cracks, and not to increase in the grain contact area/stiffness as mainly considered in this paper. A model accounting for the effect of microcrack closure, introducing microstructural parameters that describe the behavior of microfractures, has been recently presented by Katsuki et al. (2014). The model assumes randomly oriented microfractures within the rock mass, where the average fracture spacing is indicated by the letter s. The normal stiffness of microfractures k_n is

$$k_n = k_{ni}\left(\frac{\sigma'_n}{\sigma'_{ni}}\right)^n, \tag{A-1}$$

where k_{ni} is the normal stiffness of the fracture at reference normal effective stress σ'_{ni}, σ'_n is the effective stress normal to the microfracture, and n is an empirical parameter accounting for stiffness increase upon crack closure. The shear stiffness of microfractures is k_s

$$k_s = k_{si} + k_{sn}\left(\frac{\sigma'_n}{\sigma'_{ni}} - 1\right), \tag{A-2}$$

where k_{si} is the shear stiffness of the fracture at reference stress, and k_{sn} is the rate of shear stiffness increase with stress, assumed to be linear.

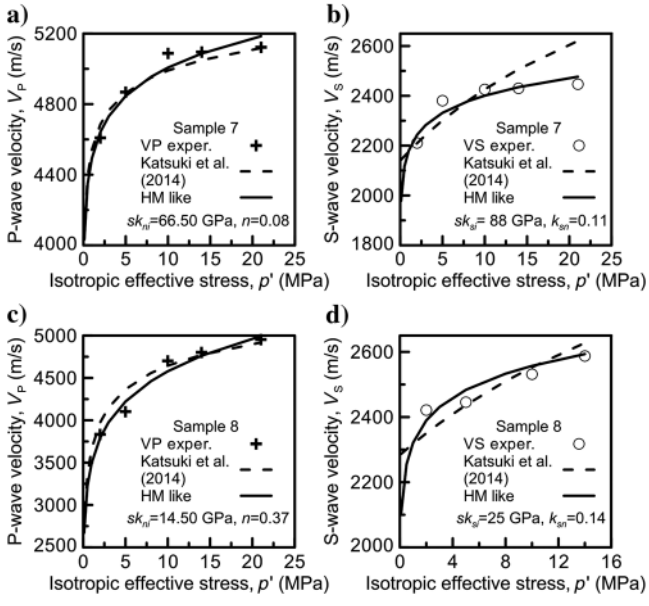

Figure A-1. Comparison between experimental data and predictions based on a Hertz-Mindlin-like formulation and Katsuki et al. (2014) formulation for two samples of case history 3. (a and c) P-wave velocities and (b and d) S-wave velocities.

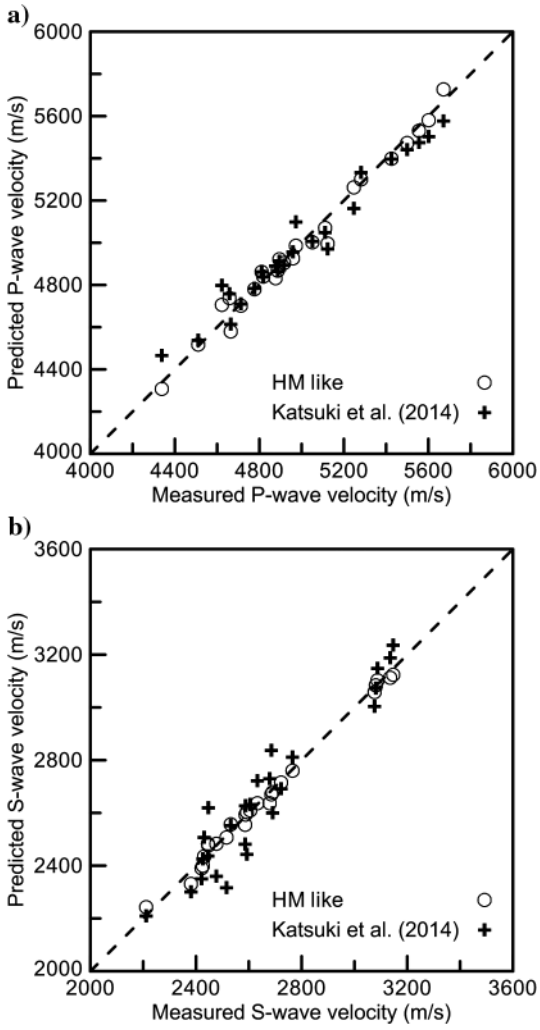

Figure A-2. Comparison between (a) P- and (b) S-wave velocities as predicted by the Hertz-Mindlin-like formula used in this study and by the Katsuki et al. (2014) formulation. Predictions refer to the whole data set of case history 3.

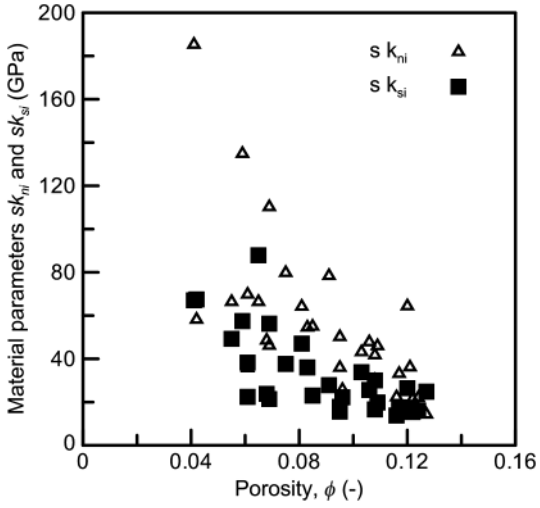

Figure A-3. Relationship between parameter sk_{ni} and sk_{si} of the formulation of Katsuki et al. (2014) with porosity for the data set of case history 3.

For a rock loaded in oedometer conditions, the P-wave velocity is given by

$$V_P = V_{Pm}\sqrt{\frac{f_n(p'_{nor})}{1+f_n(p'_{nor})}},$$
$$f_n(p'_{nor}) = \frac{2}{1+K_0}\times\frac{sk_{ni}p'^{n}_{nor}}{M_m}, \quad \text{(A-3)}$$

where V_{Pm} is the P-wave velocity in the rock mineral, K_0 is the coefficient of earth pressure at rest, and M_m is the longitudinal modulus of the mineral ($V_{Pm} = \sqrt{M_m/\rho}$). The S-wave velocity is

$$V_S = V_{Sm}\sqrt{\frac{f_s(p'_{nor})}{1+f_s(p'_{nor})}},$$
$$f_n(p'_{nor}) = \frac{s[k_{si}+k_{sn}(p'_{nor}-1)]}{G_m}, \quad \text{(A-4)}$$

where V_{Sm} and G_m are the S-wave velocity and the shear modulus of the mineral ($V_{Sm} = \sqrt{G_m/\rho}$).

Equations A-3 and A-4 were then used to interpret laboratory results from the third case history, and parameters sk_{ni}, n, as well as sk_{si} and sk_{sn} were evaluated through back analysis for each test. Figure A-1 shows the interpretation of results obtained on two samples for P- and S-wave velocities, together with the Hertz-Mindlin-like interpretation used in this work. As for P-waves, there is an almost complete overlap of the trend given by the two different expressions used. Larger (although still limited) differences are found for S-waves. Figure A-2 compares all the measurements of the data set from case history 3 with the predictions obtained with equation 1 and those obtained with the model of Katsuki et al. (2014). Results suggest that material behavior is well represented by both models. Also note from Figure A-3 that parameters sk_{ni} and sk_{si} tend to decrease as the porosity of samples increases, as was the case with the function $F_i(\phi)$ used in this study.

APPENDIX B

EXPERIMENTAL VERIFICATION OF FLUID SUBSTITUTION APPLICABILITY

The fluid substitution theory, based on the Biot-Gassmann model (Gassmann, 1951), provides a methodology to predict seismic velocities in rocks saturated with a fluid from velocities for the same rock at different saturation conditions (saturated with a different fluid or dry). It represents a widely used tool in rock physics for the analysis of sonic data from log and lab tests, as well as for the processing of seismic data at field scale. This model assumes that the shear modulus is independent of the nature of the saturating fluid, as long as the latter is not viscous. The bulk modulus of the saturated rock as a function of the parameters of the rock frame and of the saturating fluids can be expressed as

$$G_{sat} = G_{sk}, \quad \text{(B-1)}$$

$$K_{\text{sat}} = K_{sk}\frac{\left(1+\frac{K_{sk}}{K_g}\right)^2}{\frac{\phi}{K_{\text{fl}}}+\frac{1-\phi}{K_g}-\frac{K_{sk}}{K_g^2}}, \tag{B-2}$$

where G_{sat} is the shear stiffness of the saturated rock, G_{sk} is the shear stiffness of dry rock, K_{sk} is the skeleton bulk modulus (dry rock), K_g is the bulk modulus of the mineral constituting the rock, K_{fl} is the bulk modulus of the pore fluid, and ϕ is the porosity.

When two or more different fluids are present in the pore space, K_{fl} can be calculated as the a Reuss average of fluid modulus (Mavko et al., 2009):

$$\frac{1}{K_{\text{fl}}} = \sum_i \frac{S_i}{K_{\text{fl},i}}, \tag{B-3}$$

where S_i and $K_{\text{fl},i}$ are, respectively, the degree of saturation and the bulk modulus of the ith fluid phase.

Gassmann's equation is valid only at low frequencies, such that the induced pore pressures are equilibrated throughout the pore space (i.e., there is sufficient time for the pore fluid to flow and dissipate wave-induced pore pressure gradients). The use of the Biot-Gassmann formulation may not be appropriate for shale or coal formations. Indeed, shale contains bound water, which is essentially immobile, and thus cannot be in hydraulic equilibrium with the rest of the pore space. Alternative approaches can be found in the literature to overcome this problem. For example, Dvorkin et al. (2007) propose the use of an effective porosity.

Gassmann's equation requires several additional assumptions, among which the homogeneity and isotropy of the formation at the micro- and macroscales and the connectivity of the pore system. It is not possible to assess theoretically the validity of each assumption and the consequence of its potential violation. Hence, the method can only be validated by experimental testing (Grochau and Gurevich, 2009).

The most direct way to estimate the validity of Gassmann's fluid substitution is to compare moduli obtained from laboratory seismic velocities on dry samples with velocities obtained from measures on the same samples in completely or partially saturated condition after fluid substitution is operated. This approach has been applied to the ultrasonic laboratory seismic velocities of the third case history presented in the paper.

In Figure B-1a, the shear moduli obtained from S-wave ultrasonic velocities measured at a different isotropic pressure on a dry sample are compared with the corresponding moduli obtained using Gassmann's fluid substitution on measurements performed on the same sample saturated with brine and with oil. A fluid-dependency of shear moduli is also visible, although the Biot-Gassmann model predicts that the shear modulus will remain constant under different saturation. Several authors have, however, observed S-wave velocities for water saturation lower than for oil saturation (e.g., King, 1966; Khazanehdari and McCann, 2005). Other authors have observed increases in shear velocity with liquid saturation (e.g., Han et al., 1986; Khazanehdari and McCann, 2005). Khazanehdari and Sothcott (2003) compile rock-fluid interactions that explain the rock shear modulus variability with fluid. They define *rock weakening* when $G_{\text{sat}} < G_{\text{dry}}$ and *rock strengthening* for $G_{\text{sat}} > G_{\text{dry}}$. They also identify several potential mechanisms responsible for the change in shear modulus upon liquid saturation (viscous coupling, reduction in free surface energy, and dispersion due to local and global flow). According to their observations, viscous coupling and reduction in free-surface energy mechanisms show some degree of pressure dependence, being more relevant at low pressures (when fracture and pores are open). Indeed, open microfractures and low-aspect-ratio pores produce a larger surface area for fluid-solid interaction to take place. Increasing effective pressure results in closure of low-aspect ratio pores and consequently reduces the available surface area of minerals to fluids, minimizing the solid-fluid interaction. This aspect is also shown in Figure B-1a, where for increasing effective pressure a reduction in the difference between dry and saturated shear moduli is observed.

For the experimental data reported in that paper, it is, however, possible to note that, even if a trend is observable with varying saturation, the maximum difference between the dry and saturated shear moduli is less than 5%, within the limit of accuracy of the measurements (typically, a few percent on the moduli, that is to say, half of this range for the velocities). The same comparison in terms of the bulk moduli is shown in Figure B-1b.

The results show on average a good agreement between the elastic moduli computed using Gassmann's equation with the corresponding moduli directly obtained with ultrasonic velocity tests on the dry sample. This confirms that all the assumptions of the

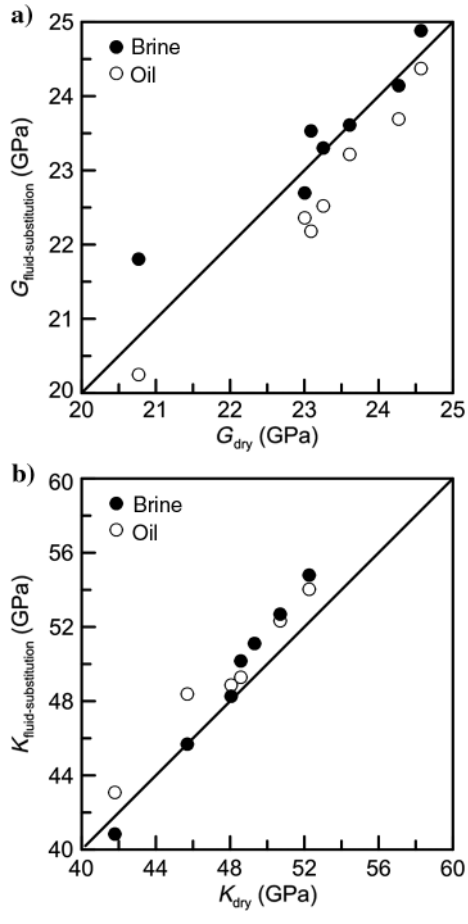

Figure B-1. Comparison between (a) shear dry moduli and (b) bulk dry moduli from ultrasonic tests with moduli predicted using Gassmann's equation on brine- and oil-saturated samples, for the data set of case history 3.

Gassmann's model are adequate within the measurement error and natural variability of elastic properties for the reported case history.

APPENDIX C

DEFINITION OF A DAMAGE INDEX ACCOUNTING FOR POROSITY CHANGE EFFECTS

A modified α_i^{pseudo} can be defined using core porosity, if available, in place of log porosity in the proposed formulation. Its use in equation 5 leads to a different index, that we shall call *DI* (damage index). This index accounts also for the effects of porosity changes at reference pressure induced by coring (or reversely, for porosity differences between sample and formation due to faults or fractures at the megascale). Whereas *SI* compares structural effects on elastic velocity within the formation with those detected on the whole sample data set at the imposed local porosity of the well, *DI* provides the expected ratio of elastic wave velocities at reference conditions between the formation and the sample proceeding from the same depth. Loss of structure leads to higher porosity at reference pressure and to slower elastic velocity-porosity trends. If damage is caused only by coring, *DI* will be a lower bound to *SI*; if damage occurred in situ because of megastructural effects (faults or fractures), *DI* will be an upper bound to *SI*. Therefore, one of the following holds: $DI \leq SI \leq 1$ or $DI \geq SI \geq 1$. When no destructuration is occurring, $DI = SI = 1$. When coring and fractures are playing a significant role, DI might actually not be a bound to *SI* because although the sample would experience a porosity increase because of alterations induced by coring, related effects might be compensated by its velocity-porosity trend laying above that of the formation.

The indices *DI* and *SI* for case histories 2 and 3 are compared in Figure C-1. As for case history 2, being core porosity higher than log porosity, DI is consistently lower than *SI* for case history 3, the opposite mostly holds. Also, it can be noticed that the difference between the two indexes is generally relatively small, and *SI* has the practical advantage of being available over larger intervals.

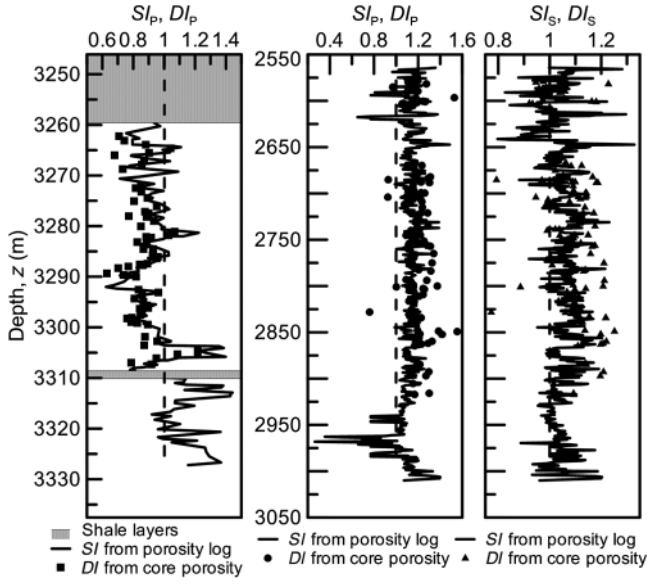

Figure C-1. Comparison between *SI* and *DI* indexes for the (a) case history 2 and for (b and c) case history 3.

REFERENCES

Alvarado, G., M. R. Coop, and S. Willson, 2012, On the role of bond breakage due to unloading in the behaviour of weak sandstones: Géotechnique, **62**, 303–316, doi: 10.1680/geot.8.P.017.

Asgharzadeh, M., A. Bóna, R. Pevzner, M. Urosevic, and B. Gurevich, 2013, Reliability of the slowness and slowness-polarization methods for anisotropy estimation in VTI media from 3C walkaway VSP data: Geophysics, **78**, no. 5, WC93–WC102, doi: 10.1190/geo2012-0409.1.

Avseth, P., T. Mukerji, G. Mavko, and J. Dvorkin, 2010, Rock physics diagnostics of depositional texture, diagenetic alterations and reservoir heterogeneity in high-porosity siliciclastic sediments and rocks — A review of selected models and suggested work flows: Geophysics, **75**, no. 5, 75A31–75A47, doi: 10.1190/1.3483770.

Berge, P. A., J. G. Berryman, and B. P. Bonner, 1993, Influence of microstructure on rock elastic properties: Geophysical Research Letters, **20**, 2619–2622, doi: 10.1029/93GL03131.

Biot, M. A., 1956a, Theory of propagation of elastic waves in a fluid-saturated porous solid. Part I: Low frequency range: The Journal of the Acoustical Society of America, , **28**, 168–178, doi: 10.1121/1.1908239.

Biot, M. A., 1956b, Theory of propagation of elastic waves in a fluid-saturated porous solid. Part II: Higher-frequency range: The Journal of the Acoustical Society of America, **28**, 179–191, doi: 10.1121/1.1908241.

Brich, F., 1960, The velocity of compressional waves in rocks to 10 kilobars, Part 1: Journal of Geophysical Research, **65**, 1083–1102, doi: 10.1029/JZ065i004p01083.

Brich, F., 1961, The velocity of compressional waves in rocks to 10 kilobars, Part 2: Journal of Geophysical Research, **66**, 2199–2224, doi: 10.1029/JZ066i007p02199.

Cha, M., G. C. Cho, and J. C. Santamarina, 2009, Long-wavelength P-wave and S-wave propagation in jointed rock masses: Geophysics, **74**, no. 5, E205–E214, doi: 10.1190/1.3196240.

Crampin, S., 1985, Evaluation of anisotropy by shear-wave splitting: Geophysics, **50**, 142–152, doi: 10.1190/1.1441824.

Della Vecchia, G., A. Pandolfi, G. Musso, and G. Capasso, 2014, An analytical expression for the determination of in situ stress state from borehole data accounting for breakout size: International Journal of Rock Mechanics & Mining Sciences, **66**, 64–68.

Diallo, M. S., M. Prasad, and E. Appel, 2003, Comparison between experimental results and theoretical predictions for P-wave velocity and attenuation at ultrasonic frequency: Wave Motion, **37**, 1–16, doi: 10.1016/S0165-2125(02)00018-5.

Duncan, J. M., and C. Y. Chang, 1970, Nonlinear analysis of stress and strain in soils: Journal of the Soil Mechanics and Foundations Division, **96**, 1629–1653.

Dvorkin, J., G. Mavko, and B. Gurevich, 2007, Fluid substitution in shaley sediment using effective porosity: Geophysics, **72**, no. 3, O1–O8, doi: 10.1190/1.2565256.

Dvorkin, J., R. Nolen-Hoeksema, and A. Nur, 1994, The squirt-flow mechanism: Macroscopic description: Geophysics, **59**, 428–438, doi: 10.1190/1.1443605.

Dvorkin, J., and A. Nur, 1993, Dynamic poroelasticity: A unified model with the squirt and the Biot mechanisms: Geophysics, **58**, 524–533, doi: 10.1190/1.1443435.

Eberhardt, E., D. Stead, and B. Stimpson, 1999, Effects of sample disturbance on the stress-induced microfracturing characteristics of brittle rock: Canadian Geotechnical Journal, **36**, 239–250, doi: 10.1139/t98-109.

Eberhart-Phillips, D., D. H. Han, and M. D. Zoback, 1989, Empirical relationships among seismic velocity, effective pressure, porosity, and clay content in sandstone: Geophysics, **54**, 82–89, doi: 10.1190/1.1442580.

Ellis, D. V., and J. M. Singer, 2008, Well logging for earth scientists: Springer.

Fjær, E., 2009, Static and dynamic moduli of a weak sandstone: Geophysics, **74**, no. 2, WA103–WA112, doi: http://dx.doi.org/10.1190/1.3052113.

Fjær, E., R. M. Holt, P. Horsrud, A. M. Raaen, and R. Risnes, 2008, Petroleum related rock mechanics: Elsevier.

Freund, D., 1992, Ultrasonic compressional and shear velocities in dry clastic rocks as a function of porosity, clay content and confining pressure: Geophysical Journal International, **108**, 125–135, doi: 10.1111/j.1365-246X.1992.tb00843.x.

Gassmann, F., 1951, Über die Elastizität poröser Medien: Vierteljahrsschrift der Naturforschenden Gesellschaft, **96**, 1–23.

Grochau, M. H., and B. Gurevich, 2008, Investigation of core data reliability to support time-lapse interpretation in Campos Basin, Brazil: Geophysics, **73**, no. 2, E59–E65, doi: 10.1190/1.2821861.

Grochau, M., and B. Gurevich, 2009, Testing Gassmann fluid substitution: Sonic logs versus ultrasonic core measurements: Geophysical Prospecting, **57**, 75–79, doi: 10.1111/j.1365-2478.2008.00726.x.
Han, D. H., A. Nur, and D. Morgan, 1986, Effects of porosity and clay content on wave velocities in sandstones: Geophysics, **51**, 2093–2107, doi: 10.1190/1.1442062.
Holt, R. M., M. Brignoli, and C. J. Kenter, 2000, Core quality: Quantification of coring-induced rock alteration: International Journal of Rock Mechanics and Mining Sciences, **37**, 889–907, doi: 10.1016/S1365-1609(00)00009-5.
Katsuki, D., M. Gutierrez, and A. Almrabat, 2014, Stress-dependent elastic wave velocity of microfractured sandstone: International Journal for Numerical and Analytical Methods in Geomechanics, **38**, 441–456, doi: 10.1002/nag.2210.
Khazanehdari, J., and C. McCann, 2005, Acoustic and petrophysical relationships in low-shale sandstone reservoir rocks: Geophysical Prospecting, **53**, 447–461, doi: 10.1111/j.1365-2478.2005.00460.x.
Khazanehdari, J., and J. Sothcott, 2003, Variation in dynamic elastic shear modulus of sandstone upon fluid saturation and substitution: Geophysics, **68**, 472–481, doi: 10.1190/1.1567213.
King, M. S., 1966, Wave velocities in rocks as a function of changes in overburden pressure and pore fluid saturants: Geophysics, **31**, 50–73, doi: 10.1190/1.1439763.
Mantilla, A. E., 2002, Predicting petrophysical properties by simultaneous inversion of seismic and reservoir engineering data: Ph.D. thesis, Stanford University.
Martin, C. D., and B. Stimpson, 1994, The effect of sample disturbance on laboratory properties of Lac du Bonnet granite: Canadian Geotechnical Journal, **31**, 692–702, doi: 10.1139/t94-081.
Mavko, G., T. Mukerji, and J. Dvorkin, 2009, The rock physics handbook: Tools for seismic analysis of porous media: Cambridge University Press.
Mavko, G. M., and A. Nur, 1979, Wave attenuation in partially saturated rocks: Geophysics, **44**, 161–178, doi: 10.1190/1.1440958.
Mindlin, R. D., 1949, Compliance of elastic bodies in contact: Journal of Applied Mechanics, **16**, 259–268.
Mitchell, J. K., and K. Soga, 2005, Fundamentals of soil behavior: John Wiley & Sons.
Murphy, W. F. III, K. W. Winkler, and R. L. Kleinberg, 1986, Acoustic relaxation in sedimentary rocks: Dependence on grain contacts and fluid saturation: Geophysics, **51**, 757–766, doi: 10.1190/1.1442128.
O'Connell, R. J., and B. Budiansky, 1974, Seismic velocities in dry and saturated cracked solids: Journal of Geophysical Research, **79**, 5412–5426, doi: 10.1029/JB079i035p05412.
Okaya, D., W. Rabbel, T. Beilecke, and J. Hasenclever, 2004, P-wave material anisotropy of tectono-metamorphic terrane: An active source seismic experiment at the KTB super-deep drill hole, southeast Germany: Geophysical Research Letters, **31**, L24620, doi: 10.1029/2004GL020855.
Peng, Z., and Y. Ben-Zion, 2004, Systematic analysis of crustal anisotropy along the Karadere-Düzce branch of the North Anatolian fault: Geophysical Journal International, **159**, 253–274, doi: 10.1111/j.1365-246X.2004.02379.x.
Puzrin, A. M., and J. B. Burland, 1996, A logarithmic stress-strain function for rocks and soils: Géotechnique, **46**, 157–164, doi: 10.1680/geot.1996.46.1.157.
Ramberg, W., and W. R. Osgood, 1943, Description of stress-strain curves by three parameters: Technical note no. 902, National Advisory Committee For Aeronautics.
Rasolofosaon, P. N. J., and B. Zinszner, 2012, Experimental verification of the petroelastic model in the laboratory — Fluid substitution and pressure effects: Oil & Gas Science and Technology — Revue d'IFP Energies nouvelles, **67**, 303–318.
Santamarina, J. C., K. A. Klein, and M. A. Fam, 2001, Soils and waves: Particulate materials behavior, characterization and process monitoring: John Wiley & Sons.
Savage, M. K., 1999, Seismic anisotropy and mantle deformation: What have we learned from shear wave splitting?: Reviews of Geophysics, **37**, 65–106, doi: 10.1029/98RG02075.
Walsh, J. B., 1965a, The effect of cracks on the compressibility of rocks: Journal of Geophysical Research, **70**, 381–389, doi: 10.1029/JZ070i002p00381.
Walsh, J. B., 1965b, The effect of cracks on the uniaxial compression of rocks: Journal of Geophysical Research, **70**, 399–411, doi: 10.1029/JZ070i002p00399.
Wang, Q., S. Ji, M. H. Salisbury, B. Xia, M. Pan, and Z. Xu, 2005, Pressure dependence and anisotropy of P-wave velocities in ultrahigh-pressure metamorphic rocks from the Dabie-Sulu orogenic belt (China): Implications for seismic properties of subducted slabs and origin of mantle reflections: Tectonophysics, **398**, 67–99, doi: 10.1016/j.tecto.2004.12.001.
Zimmerman, R. W., W. H. Somerton, and M. S. King, 1986, Compressibility of porous rocks: Journal of Geophysical Research: Solid Earth (1978–2012), **91**, 12765–12777.
Zoback, M. D., D. Moos, L. Mastin, and R. N. Anderson, 1985, Well bore breakouts and in situ stress: Journal of Geophysical Research, **90**, 5523–5530, doi: 10.1029/JB090iB07p05523.